Published in final edited form as:

*Exp Mech*. 2017 January ; 57(1): 155–163. doi:10.1007/s11340-016-0202-x.

# Designing a Uniaxial Tension/Compression Test for Springback Analysis in High-Strength Steel Sheets

**M. R. Stoudt**[*], **L. E. Levine**, and **L. Ma**

National Institute of Standards & Technology, 100 Bureau Drive, Gaithersburg, MD 20899

## Abstract

We describe an innovative design for an in-plane measurement technique that subjects thin sheet metal specimens to bidirectional loading. The goal of this measurement is to provide the critical performance data necessary to validate complex predictions of the work hardening behavior during reversed uniaxial deformation. In this approach, all of the principal forces applied to the specimen are continually measured in real-time throughout the test. This includes the lateral forces that are required to prevent out of plane displacements in the specimen that promote buckling. This additional information will, in turn, improve the accuracy of the compensation for the friction generated between the anti-bucking guides and the specimen during compression. The results from an initial series of experiments not only demonstrate that our approach is feasible, but that it generates data with the accuracy necessary to quantify the directionally-dependent changes in the yield behavior that occur when the strain path is reversed (i.e., the Bauschinger Effect).

### Keywords

Bauschinger Effect; Yield Phenomena; Residual Stresses; Ferritic steels; Springback

## 1. Introduction

Throughout the transportation industry, the need to reduce vehicle weight and improve fuel economy has heightened the demand for new lightweight sheet alloys such as aluminum, magnesium, and advanced high strength steels (AHSS). However, the property data and constitutive laws available for many of these alloys are limited or inadequate for the complex models that are used to predict the performance. Specifically, the lack of property data leads to inaccurate results in the predicted mechanical response to the applied loads generated during sheet metal forming. The ensuing inability to accurately predict the mechanical behavior impedes widespread incorporation of these advanced alloys in vehicles.

Springback (defined as a change in the component shape caused by elastic unloading after forming) is one of the most challenging behaviors to model in metal forming. It is generally attributed to a non-uniform distribution of residual stresses generated by complex loading conditions during stretch forming. Many approaches have been adopted to predict the changes in shape that occur after the forming loads have been removed [1–4]. However,

[*]Corresponding Author. Phone: (301) 975-6025, Fax: (301) 975-4553, stoudt@nist.gov.

predicting springback is particularly problematic because many of these models require a detailed assessment that describes how the stress distribution is influenced by the microstructure of the material [5]. Such an assessment can be extremely difficult to acquire because the microstructures of AHSS are usually multi-phase and often contain metastable phases that can transform under certain stress conditions. While the complex microstructures significantly enhance the strength of these alloys, they also introduce a strong directional dependence in the mechanical properties. This directional dependence exacerbates forming issues such as springback.

Under complex loading, most polycrystalline materials exhibit a directional dependence in the yield stress to some extent [6]. This behavior is largely referred to as the Bauschinger Effect (BE), and it is known to have a strong influence on the magnitude of the springback [7]. Yoshida, et al [8], showed that the BE consists of three general phenomena. These are: 1) the initial re-yielding, which typically manifests as a decrease in the observed yield stress after the loading direction has been reversed, 2) the transient BE, which generally occurs after the reversed applied stress has changed from tensile to compressive, and 3) the permanent softening, which occurs after the transient BE has saturated and the dislocations in the structure begin to annihilate one another. The physical mechanism that produces the Bauschinger effect is debatable, but it is frequently described as an inherent directionality of the dislocation structures that accumulate at barriers within a deformed polycrystalline material [9]. Two primary dislocation-level models have been developed to describe the BE. These are: a) the Mughrabi composite model [10], and b) the Orowan–Sleeswyk model [11]. The fundamentals for both mechanisms are detailed in a review of the microstructural origins of the Bauschinger effect recently published by Kassner et al [12].

Generating the data to refine the models used to predict springback requires highly specialized test methods. Most deformation modeling assumes isotropic hardening, where the yield surface expands equally in all directions as the material deforms [13]. A second common assumption for hardening is kinematic hardening, where the yield surface translates in the direction of the applied load, but does not expand [14,15]. Models based exclusively on isotropic hardening or on kinematic hardening are often insufficient because real materials typically exhibit a combination of isotropic expansion, kinematic translation and anisotropic expansion where one quadrant of the yield locus expands faster than another [16]. For this reason, property measurements under reversed loading are needed to quantify the active hardening mechanisms in the response of a given material and then relate those characteristics to the underlying microstructure. These relationships can be used to improve the predicted response of that material to complex loading schemes [17]. While several test methods have been developed for this purpose [18,8,19,20], bidirectional, in-plane testing of thin sheet is the preferred method because it produces more homogeneous stress/strain distributions in the gauge area of the specimen. This also facilitates more accurate assessments of the residual stress distribution.

An assessment of the limited number of anti-buckling systems described in the literature for use in reversed uniaxial loading revealed that the designs fall into two general categories. The first category fixes the displacement between the specimen and the anti-buckling (AB) guide, thereby making the corresponding force between the two an un-measurable variable

[20]. During tension, these designs allow a small gap to develop between the specimen and the AB guides as the specimen thins. During compression, this gap enables the nucleation of a small out-of-plane displacement, which in turn, requires an exceptionally high amount of lateral force to prevent it from propagating and producing a buckle in the gauge section of the specimen. The size and influence of the gap can be reduced with proper calibration, but with this approach, there is no way to adjust the system during a live test. The second design category is a clam shell-type AB apparatus that essentially clamps onto the gauge area. The restoring force is typically supplied by a series of springs that are torqued to a pre-set level and the magnitude of the applied force is estimated from the linear spring constants. This approach produces a constant net applied force on the specimen; but depending on the shape of the AB guide, it could also allow the specimen to bend in the grips or permit the development of a small gap between the AB guides and the specimen that could initiate a buckle. The main concern with this approach is that this apparatus is attached to the specimen prior to the test and remains in contact with the specimen throughout the test. This applies an unnecessary frictional force to the specimen during the tensile segment that requires extensive calibration for compensation. Based on this assessment, the optimum AB guide design would produce a variable lateral force system that minimizes the friction on the specimen during the test. That is, it would remove or reduce the lateral forces when they are not needed, and it would allow for adjustment (balancing) of the lateral forces in real-time during compression.

## 2. Design

Regardless of the approach adopted, accurate compensation for the friction generated between the lateral constraints, required to prevent buckling, and the gauge section of the specimen during compression is a considerable design challenge. Our objective was to develop a fully instrumented anti-buckling apparatus that measures all of the primary forces applied to a thin sheet specimen throughout the test. As such, the lateral forces applied to the AB guides are continuously sampled in real-time. This will enable direct assessment of the contact forces, which in turn, will improve the accuracy of the friction correction. Fig. 1a is a computer-aided design (CAD) drawing of the apparatus showing the arrangement of the major components in our design. As shown in the figure, the key element is two opposing high-precision piezoelectric actuators (#1 in the figure) that operate in dynamic closed-loop displacement control to simultaneously apply the forces on the anti-buckling (AB) guides. Small, high-capacity load cells mounted behind each actuator measure the applied lateral force. Each actuator can apply 30 kN (6.7 kip) of force over a 120 μm ($4.72\times10^{-3}$ in) travel, and because it operates independently in closed-loop control, each actuator can maintain a set position with an accuracy of ±1 nm. This allows the actuators to rapidly adjust and balance the lateral forces on the anti-buckling guides as required throughout the test. Each actuator is housed in a conical holder (#2) that supports the weight of the actuators with no appreciable bending, and aids in transferring the lateral reaction forces to the frame (#3). The frame itself consists of two steel plates that were precision-ground to maintain a surface flatness that did not deviate more than 0.0127 mm (0.0005 in). The distance between the plates was fixed by four precision-ground sleeve assemblies (#4), and while the frame was

pre-loaded to 136 N·m (100 lb·ft) by those assemblies, the spacing between the plates did not vary more than 0.00254 mm (0.0001 in) at the maximum applied lateral force.

A close-up view of the high-precision system used to apply the lateral forces to the specimen is shown in Fig. 1b. The AB guides (#5 in the figure) are positioned on either side of the test specimen. Guide pins were positioned in the tab sections to prevent rotation and maintain the planar alignment of the AB guides. The widths of the AB guides were designed to be 0.5 mm (0.019 in) less than the specimen gauge width after the application of 0.08 tensile strain to facilitate high-resolution strain measurements by digital image correlation (DIC). Precision-ground cemented tungsten carbide (CWC) push rods (#6) transmit the force from the piezoelectric actuator to the AB guides. These 600+ GPa ($87\times10^6$ psi) elastic modulus rods were specifically designed to minimize the compliance between the actuator and the AB guides during the application of force. Even though the actuators are capable of applying 30 kN, this can only be an axial force. The quartz crystals in the piezoelectric stack would fracture if they experience an out-of-plane force greater than 140 N (31.5 lbf). Consequently, each CWC push rod is encased in a high-precision linear bearing (#7) that centers the rod on a hemispherical cap mounted on the actuator with zero out-of-plane displacement. Fig. 2 is a photograph of the fully assembled AB apparatus inside the servo-hydraulic test frame.

Deforming a thin sheet specimen to large strains in compression and then in tension requires a highly specialized specimen design, even when using AB guides. During compression, a thin sheet specimen basically fails in one of three possible modes: a) a collapse in the unsupported region of the tab located between the AB guides and the grips, referred to as an ‘L-buckle’, b) a collapse in the gauge area that produces a rotation along the gauge length, referred to as a ‘W-buckle’ and c) a through-the-thickness collapse in the gauge area with no rotation, referred to as a ‘T-buckle’. The specimen geometry suppresses the W and L-buckling modes and promotes a T-buckle because this mode can be prevented by the application of appropriate lateral force with the AB guide. As such, we developed a finite element analysis (FEA) model similar in concept to that used by Boger, *et al* [19] to predict the deformation of a suitable specimen geometry in fully-reversed uniaxial loading, and then to optimize the specimen geometry for a range of strain levels and materials. Our model was based on the commercial FEA code ABAQUS[1] and used isotropic hardening with both fixed and variable lateral forces to predict the performance at the upper bound for a range of test conditions.

The specimen geometry, mesh and boundary conditions are shown in Fig. 3. The model used parametric inputs to vary the specimen geometry parameters including: the width of the grip region, B, the uniform gauge section length, G, the uniform gauge section width, W, the transition radius, R, and the thickness of the gap between the specimen and the AB guide, L. The initial thickness of the specimen was 1 mm for all of the simulations. The AB guides were initially modeled as rigid plates that were in contact with the specimen. Each reference point of the lateral rigid plates was connected to a spring element to simulate the lateral

[1]Certain commercial entities, equipment, or materials may be identified in this document in order to describe an experimental procedure or concept adequately. Such identification is not intended to imply recommendation or endorsement by the National Institute of Standards and Technology, nor is it intended to imply that the entities, materials, or equipment are necessarily the best available for the purpose.

force applied by the piezoelectric actuator. The stiffness of the spring element was designed to emulate the load displacement relationship of the piezoelectric actuator. The rigid plates were only allowed to move in the z direction, which was perpendicular to the specimen surfaces. During the simulation, the positions of the bottom grip surface nodes were fixed, and the top grip surface nodes were only allowed to move in the *y* direction. Uniaxial displacements sufficient to produce a fully reversed 0.08 strain were added to the top grip surface nodes. Four nodes (the red dots in the specimen gauge area in Fig. 3) were positioned along the center line of specimen at distances of ± 6.25 mm (0.25 in) and ± 12.5 mm (0.49 in) from the midpoint of the specimen to serve as strain gauge reference points. In the simulation, the specimen was first uniaxially compressed to the point where the displacement between the reference nodes produced −0.08 true strain, after which the specimen was pulled in tension to where the displacement between the nodes resulted in a +0.08 strain. Once this condition was achieved, the specimen was then again compressed to where the displacements between the nodes were equal to their initial positions (i.e., zero net strain). The FEA model tracked the percentage of the fully reversed uniaxial cycle completed during the simulation. The specimen geometry was considered to be acceptable if the distribution of the simulated strain was uniform in the region of the gauge section bounded by the 12.5 mm nodes over the range of the ± 0.08 strain cycle. Additional optimizations were performed on the set of acceptable geometries to produce a suitable final specimen geometry.

Fig. 4 compares the end points of two FEA simulations of sample behavior for two different specimen geometries under a full ± 0.08 strain cycle in DP600 steel. Numerous simulations of this type were run until an acceptable geometry was identified. In the figure, G is the gauge length, W is the gauge width and R is the radius (all dimensions are in millimeters). The G37W15R5 geometry (Fig. 4a) failed inside the dotted ellipse prior to completion, whereas the G27W24R10 geometry in Fig. 4b successfully completed the cycle. Note that the total accumulated strain produced in the specimen during these simulations was 0.32. As such, the simulation was considered as an upper bound in the performance of a candidate geometry because, as noted previously, these simulations only assumed isotropic hardening. In real materials, strain softening via dislocation annihilation is known to occur when the strain path is reversed [21,22], which reduces the intensity of the localized work hardening and extends the overall life of the specimen [23]. The G27W24R10 geometry was then further optimized and scaled to feature an overall length of 190 mm (7.5 in), a uniform gauge section of (47 × 24) mm (1.85 × 0.94) in, a tab width of 44 mm (1.73 in), and a radius of 10 mm (0.39 in).

## 3. Experimental

The critical element in this experiment is the alignment of the lateral forces with respect to the plane of the specimen. Without proper alignment, balancing of the two lateral forces during compression is virtually impossible, and this would result in out of plane bending that promotes buckling. The high-precision alignment was accomplished in two steps. The frame was first coarse-aligned by adjusting the position relative to gauge blocks and reference marks. Precision alignment was achieved by elastically loading a 5 mm thick precision-ground reference specimen in the hydraulic grips. Gold-coated optical flats, mounted on the

specimen at the point where the center of the AB guide would contact the test specimen, provided fixed reference points. An autocollimator assembly with a lateral resolution of ± 0.0014° (5 arc seconds) was then inserted into a piezoelectric cell holder. The frame orientation was adjusted relative to the autocollimator signal by turning one of three 1/4–80-thread positioners located in the bottom of the frame until the orientation error was less than 0.01°.

Test specimens in the G27W24R10 geometry were cut from 1 mm (0.039 in) thick AISI-1008 and DP600 AHSS sheet with a water-jet. The specimens were de-burred and sanded with fine emery paper to remove any surface oxides prior to testing. The bi-directional test consisted of loading the specimen in the hydraulic grips and positioning the AB guides against the sample. The guides were designed to fix the height of the unsupported region between the grips and the sample at precisely 5 mm (0.197 in). A light film of lubricant was applied to ultra-high molecular weight polyethylene anti-friction pads prior to closing the guides. An elastic tensile preload was applied to the specimen to ensure proper sample alignment before closing the AB guides. Next, a nominal preload of 1.5 kN (337 lbf) was applied to the AB guides using coarse positioners. The piezoelectric actuators were then extended until the force on each side of the AB guides was approximately 2.2 kN (495 lbf). This force was determined empirically through a series of calibration experiments and was used for all experiments.

A series of proof of concept experiments was conducted to evaluate the performance of the AB apparatus using real specimens under actual loading conditions. It was also intended to determine the efficacy of the independently actuating, position-controlled lateral force measurement system. During these initial performance evaluations, the strain range was limited to ± 0.04 and the experiments were conducted exclusively in position control. This allowed for a thorough assessment of both the software designed to control the AB system, and the suitability of the specimen design under the fully-reversed loading without generating excessive forces on the AB guides, which could cause catastrophic results. Subsequent experiments achieved full loop strain ranges of ± 0.06 with an overall design maximum of ±0.08.

The yielding behaviors of two steels with substantially different strength levels were evaluated in fully-reversed loading. A specimen with the optimized G27W24R10 geometry was first loaded in compression at a constant displacement rate that produced an initial strain rate of $\dot{\varepsilon} \approx 3.36\times10^{-4}\ s^{-1}$. When the output of the extensometer that was mounted on the specimen edge indicated that a strain of −0.04 was achieved, the test was paused to reduce the forces on the AB guides and then resumed until a tensile strain of +0.04 was attained. The test was again paused to reapply the lateral forces. The specimen was reloaded in compression until zero strain was reached, thereby completing the test.

The actual applied strain levels were verified with a three dimensional digital image correlation (DIC) measurement system. A representative strain distribution, which was derived from the DIC data using the Hencky elasticity model [24], is shown for the ±0.04 strain cycle in Fig. 5. In the figure, the maximum strain for the tension segment (Fig. 5A) occurred in the middle of the gauge section, but the maximum strain was more diffuse

during the compression segment (Fig. 5B). In this part of the experiment, the maximum strain occurred closer to the actuator, which can be seen at the bottom of the figure.

## 4. Results and Discussion

The microstructures of the two steels are shown in Fig. 6. The AISI-1008 (Fig. 6a) is a mixture of spherodized pearlite (P) in a ferrite ($\alpha$) matrix [25]. The DP600 (Fig. 6b) is a ferrite matrix ($\alpha$) populated with islands of martensite (M), which is typically achieved by rapidly quenching low carbon steel from a temperature that is above $Ac_1$ but below $Ac_3$ (the ferrite-to-austenite transformation start and finish temperatures, respectively) on a continuous cooling transformation diagram [26]. The carbon contents for the two steels are essentially the same (0.085 C for AISI-1008 versus 0.090 C for DP600); however, the microstructures of the two steels are considerably different. Both steels have two-phase microstructures; however, the finer grain size and the martensite enhance the overall strength of the DP600 [26]. This is reflected in both the nominal yield and ultimate tensile stresses for the AISI-1008 steel, which are (245 and 340) MPa (35.5 and 49.3) ksi, and (420 and 600) MPa (60.9 and 87) ksi for the DP600. The ductilities for both steels are comparable (≈ 0.2).

The measured behavior of the two steels in bidirectional loading is shown in Fig. 7. Table 1 shows the successive maximum and yield stress values based on a 0.1 % offset criterion for the true-stress-true-strain curves (points 1, 2 and 3 in the figure). Assuming perfect isotropic hardening, where the yield surface is identical in all directions, the second yield point would occur at the same magnitude stress (but opposite sign) as the previous maximum. Assuming perfect kinematic hardening with no offset in the initial yield surface, the translation of the yield surface would be equal to the difference between the maximum stress and the initial yield stress. The magnitude of the second yield stress would thus be the initial yield stress minus this translation. Using this very simple analysis, the predicted second yield in AISI-1008 is 333 MPa (48.3 ksi) for isotropic hardening and 47 MPa (9.82 ksi) for kinematic hardening. The measured yield at 165 MPa (111 ksi) establishes that the hardening is a mixture of isotropic and kinematic. In contrast, the predicted isotropic and kinematic second yield points occur in the DP600 at 711 MPa (103 ksi) and 203 MPa (29.4 ksi), respectively. The measured second yield value of 216 MPa (31.3 ksi) reveals an almost pure kinematic hardening.

We also completed a more sophisticated analysis of these data using a nonlinear isotropic/kinematic hardening model in ABAQUS [27]. Here, the yield surface is given by $F = f(\sigma - \alpha) - \sigma^0 = 0$, where $\sigma^0$ is the yield stress, and $f(\sigma - \alpha)$ is the equivalent Mises stress with respect to the back-stress, $\alpha$. The kinematic hardening component includes a purely kinematic term (linear Ziegler hardening law) and a relaxation term, which introduces the nonlinearity. Fig 7c shows our model fit for AISI-1008 and Fig 7d shows the results for DP600. In both cases, the model does an excellent job fitting the initial hardening curve in compression and the second yield in tension. The subsequent hardening during the tension cycle is overestimated due to the permanent softening in the real system. The results of these simulation agree perfectly with the simple model described above. The AISI-1008 behavior

is a mixture of kinematic and isotropic hardening, and the DP600 behavior is best modeled using pure kinematic hardening.

It is well known that the performance of any alloy is determined by the microstructure and the thermal processing [28,29]. The two steels in this evaluation were selected specifically because they both have a have an α-ferrite matrix and similar carbon contents. While there are distinct differences in the grain size (Fig 6), which will contribute to the overall mechanical behavior (i.e., the Hall-Petch effect), that influence is expected to be small with respect to the property differences caused by the second phase constituents. Since the carbon contents in the two steels are essentially the same, it is reasonable to assume that the relative strengths of the ferrite phases are also similar. For this reason, the difference in the yield behaviors exhibited in Fig 7 can be primarily attributed to the differences in the strength of the pearlite in the 1008 and the martensite in the DP600. This is completely consistent with the findings of Allain and Bouaziz [5] who showed that kinematic hardening is largely caused by incompatibilities in the relative strengths of the constituent phases present. Their results revealed that DP steels exhibit mostly kinematic hardening because of the large local property gradients existing between the α-ferrite and the martensite. They also showed that ferrite-pearlite steels tend to exhibit a large BE, but the property gradient between the ferrite and pearlite will be less severe. Hence, the hardening in these steels will be a mixture of isotropic and kinematic hardening and the ratio will depend on the α-ferrite/pearlite phase fractions.

As noted previously, our design enables sampling of all the applied forces in real time throughout the test. Measuring both the lateral and axial forces in real time enables a determination of the instantaneous coefficient of the dynamic friction, $\mu_k$. Since this coefficient is dimensionless, the friction values are not specific to the size of the specimen used in the test. The variation in dynamic friction is shown as a function of the elapsed test time in Fig 8. The coefficient of dynamic (kinetic) friction, $\mu_k$, is given by $\mu_k = \frac{(F_B - F_T)}{(F_R + F_L)}$, where $F_B$ and $F_T$ are the bottom and top forces, respectively, and the right and left lateral forces are $F_R$ and $F_L$, respectively. The largest measured $\mu_k$ observed in these experiments was approximately 0.25, and this was a transient that occurred during switchover from compression to tension when the anti-buckling guides were retracted. The maximum non-transient frictional force, $|F_T - F_B|$, for either steel occurred at the end of the first compression stage (Region I in Fig 8) and was approximately 0.135 for the AISI-1008, and 0.12 for the DP600. This was less than 4 % of the total applied load. Since the upper and lower load cells record the forces applied to the upper and lower parts of the sample respectively, and the AB guides and sample geometry are symmetric, we estimate from this that the applied load at the center of the specimen is: $(F_T + F_B)/2$, which produced the maximum friction correction. Note that the magnitude of $\mu_k$ is consistent with values used in typical sheet metal forming simulations [30]. More importantly, the actual effect of friction during the measurement was minimal.

The true stress in Fig 7 was obtained using this friction correction equation. These results were achieved with a maximum lateral force of approximately −2.3 kN (−517 psi), which is significantly less than the 8 kN (1800 psi) to 10 kN (2250 psi) restoring force reported in the

literature [31,19]. These low friction results validated the principal philosophy behind our design. That is, the friction between the AB guides and the specimen can be minimized by, a) ensuring highly precise alignment of the AB guides with respect to the sample, b) eliminating any gap between the AB guides and the specimen, and c) applying force to the AB guides sufficient to prevent nucleation of out-of-plane displacements (i.e., a buckle). Our FEM simulations also indicate that the formation of even the smallest gap enables nucleation of out-of-plane displacements that require substantially higher lateral forces to prevent propagation [20], and that refinement of our design and testing procedures could further reduce the contact forces making friction compensation unnecessary.

## 5. Conclusions

These experiments confirmed that our approach to subjecting a thin sheet to bidirectional uniaxial loading is viable and that our technique can be used to characterize the mechanism(s) responsible for the Bauschinger effect in AHSS and other alloys. Since the design of this anti-buckling system enables a direct assessment of the coefficient of dynamic friction, it provides a more accurate compensation for the forces, which is independent of the specimen size. The two steels examined have similar carbon contents and ductilities, but markedly different microstructures. Consequently, the difference in the yield behaviors observed in the two steels is attributed to the strength difference between the pearlite in the 1008 and the martensite in the DP600. Although the mechanisms responsible for the Bauschinger effect remain controversial, these microstructural differences clearly play a major role in the markedly different ratios of isotropic and kinematic hardening in these two steels. That is, the AISI 1008 exhibits a mixture of isotropic and kinematic hardening and, by comparison, DP600 is almost purely kinematic. These results are consistent with the literature.

## Acknowledgments

All of the work described herein was performed at the National Institute of Standards and Technology and was supported by internal funding from the Materials Science and Engineering Division. We would like to acknowledge D. J. Pitchure, of the NIST Mechanical Performance Group, for his helpful suggestions and assistance with the CAD modeling, and C. Amigo, D. Barry, B. Pries, and J. Kisner, of the NIST Fabrication Technology Group, for their collective expertise and advise offered during the fabrication of the numerous precision components in our apparatus.

## References

1. Lee M-G, Kim D, Kim C, Wenner ML, Wagoner RH, Chung K. Spring-back evaluation of automotive sheets based on isotropic-kinematic hardening laws and non-quadratic anisotropic yield functions: Part II: characterization of material properties. I. J Plasticity. 2005; 21(5):883–914.
2. Cho Y-G, Kim J-Y, Cho H-H, Cha P-R, Suh D-W, Lee JK, Han HN. Analysis of Transformation Plasticity in Steel Using a Finite Element Method Coupled with a Phase Field Model. PLoS ONE. 2012; 7(4):e35987. [PubMed: 22558295]
3. Chung K, Lee M-G, Kim D, Kim C, Wenner ML, Barlat F. Spring-back evaluation of automotive sheets based on isotropic-kinematic hardening laws and non-quadratic anisotropic yield functions: Part I: theory and formulation. I. J Plasticity. 2005; 21(5):861–882.
4. Fernandes JV, Rodrigues DM, Menezes LF, Vieira MF. A modified Swift law for prestrained materials. I. J Plasticity. 1998; 14(6):537–550.

5. Allain S, Bouaziz O. Microstructure based modeling for the mechanical behavior of ferrite–pearlite steels suitable to capture isotropic and kinematic hardening. Mater Sci and Engr: A. 2008; 496(1–2): 329–336. doi:http://dx.doi.org/10.1016/j.msea.2008.06.009.
6. Edwards EH, Washburn J, Parker ER. SOME OBSERVATIONS ON THE WORK HARDENING OF METALS. Transactions of the American Institute of Mining and Metallurgical Engineers. 1953; 197(11):1525–1529.
7. Tan Z, Magnusson C, Persson B. The Bauschinger effect in compression-tension of sheet metals. Mater Sci and Engr: A. 1994; 183(1–2):31–38.
8. Yoshida F, Uemori T, Fujiwara K. Elastic–plastic behavior of steel sheets under in-plane cyclic tension–compression at large strain. I. J Plasticity. 2002; 18(5–6):633–659.
9. Kostryzhev A, Strangwood M, Davis C. Bauschinger Effect in Microalloyed Steels: Part I. Dependence on Dislocation-Particle Interaction. Metall Mater Trans A. 2010; 41(6):1399–1408.
10. Mughrabi H. Dislocation wall and cell structures and long-range internal stresses in deformed metal crystals. Acta Mater. 1983; 31:1367–1379.
11. Sleeswyk AW, James MR, Plantinga DH, Maathius WST. Reversible strain in cyclic plastic deformation. Acta Mater. 1978; 26:1265–1271.
12. Kassner ME, Geantil P, Levine LE. Long range internal stresses in single-phase crystalline materials. I. J Plasticity. 2013; 45(0):44–60. doi:http://dx.doi.org/10.1016/j.ijplas.2012.10.003.
13. Swift HW. Plastic instability under plane stress. J Mech Phys Solids. 1952; 1(1):1–18.
14. Frederick CO, Armstrong PJ. A mathematical representation of the multiaxial Bauschinger effect. Materials at High Temperatures. 2007; 24(1):11–26.
15. Chaboche JL. A review of some plasticity and viscoplasticity constitutive theories. I. J Plasticity. 2008; 24(10):1642–1693.
16. Hosford, WF., Caddell, RM. Metal Forming: Mechanics and Metallurgy. 4. New York: Cambridge University Press; 2011.
17. Lee J-W, Lee M-G, Barlat F. Finite element modeling using homogeneous anisotropic hardening and application to spring-back prediction. I. J Plasticity. 2012; 29(0):13–41. doi:http://dx.doi.org/10.1016/j.ijplas.2011.07.007.
18. Kuwabara T. Advances in experiments on metal sheets and tubes in support of constitutive modeling and forming simulations. I. J Plasticity. 2007; 23(3):385–419.
19. Boger RK, Wagoner RH, Barlat F, Lee MG, Chung K. Continuous, large strain, tension/compression testing of sheet material. I. J Plasticity. 2005; 21(12):2319–2343. doi:http://dx.doi.org/10.1016/j.ijplas.2004.12.002.
20. Dietrich L, Turski K. New Methods of Studying Thin Sheets in Compression. Engr Trans. 1978; 26(1):91–99.
21. Essmann U, Mughrabi H. Annihilation of Dislocations During Tensile and Cyclic Deformation and Limits of Dislocation Densities. Phil Mag A. 1979; 40(2):731–756.
22. Neumann P. Dislocation Dynamics in Fatigue. Phys Scr. 1987; T19B:537–543.
23. Laird C, Buchinger L. Hardening Behavior in Fatigue. Metall Trans A. 1985; 16A:2201–2214.
24. Xiao H, Chen LS. Hencky's elasticity model and linear stress-strain relations in isotropic finite hyperelasticity. Acta Mechanica. 2002; 157(1):51–60.
25. Anon. ASM Handbook. 9th. Metals Park, OH: ASM International; 1985. ASM Handbook Volume 9: Metallography and Microstructures, vol 9.
26. Krauss, G. Steels-Processing, Structure and Performance. Metals Park, OH: ASM International; 2005.
27. Anon. Abaqus, Theory and User's Manual, Version 6.13. Providence, RI: Dassault Systèmes Simulia Corp; 2013.
28. Olson GB. Computational Design of Hierarchically Structured Materials. Science. 1997; 277(5330):1237–1242.
29. Xiong W, Olson GB. Integrated computational materials design for high-performance alloys. MRS Bulletin. 2015; 40(12):1035–1044.
30. Lanzon JM, Cardew-Hall MJ, Hodgson PD. Characterizing Frictional Behavior in Sheet Metal Forming. J Mater Proc Tech. 1998; 80(1):251–256.

31. Bae GH, Huh H. Tension/compression test of auto-body steel sheets with the variation of the pre-strain and the strain rate. Transactions on Engineering Sciences. 2011; 72:213–225.

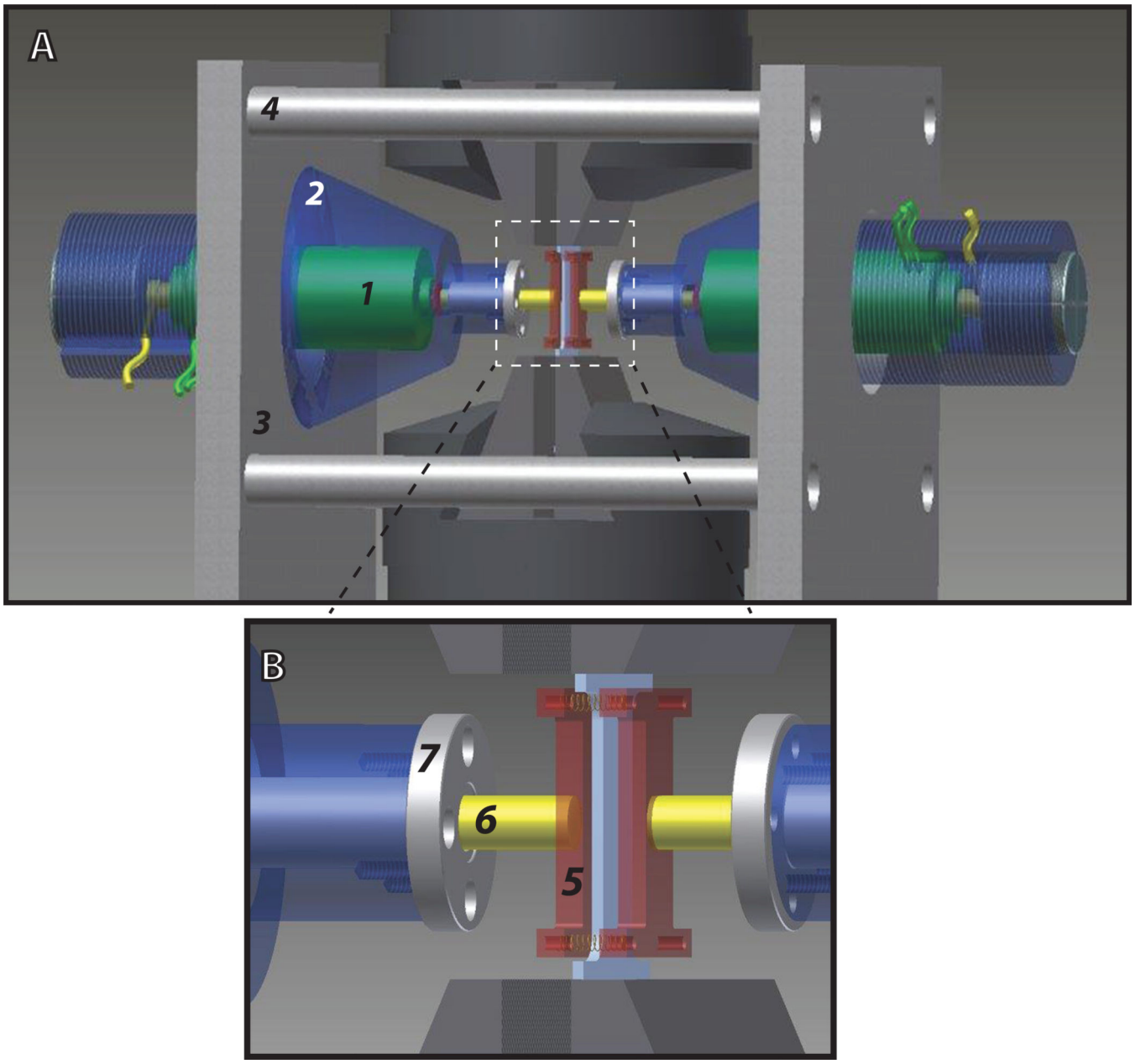


**Fig 1.**

A computer-aided design (CAD) drawing showing the layout of the anti-buckle apparatus design. The locations of the major components are shown in Fig 1a, and a larger view of the precision force application system is shown as Fig 1b

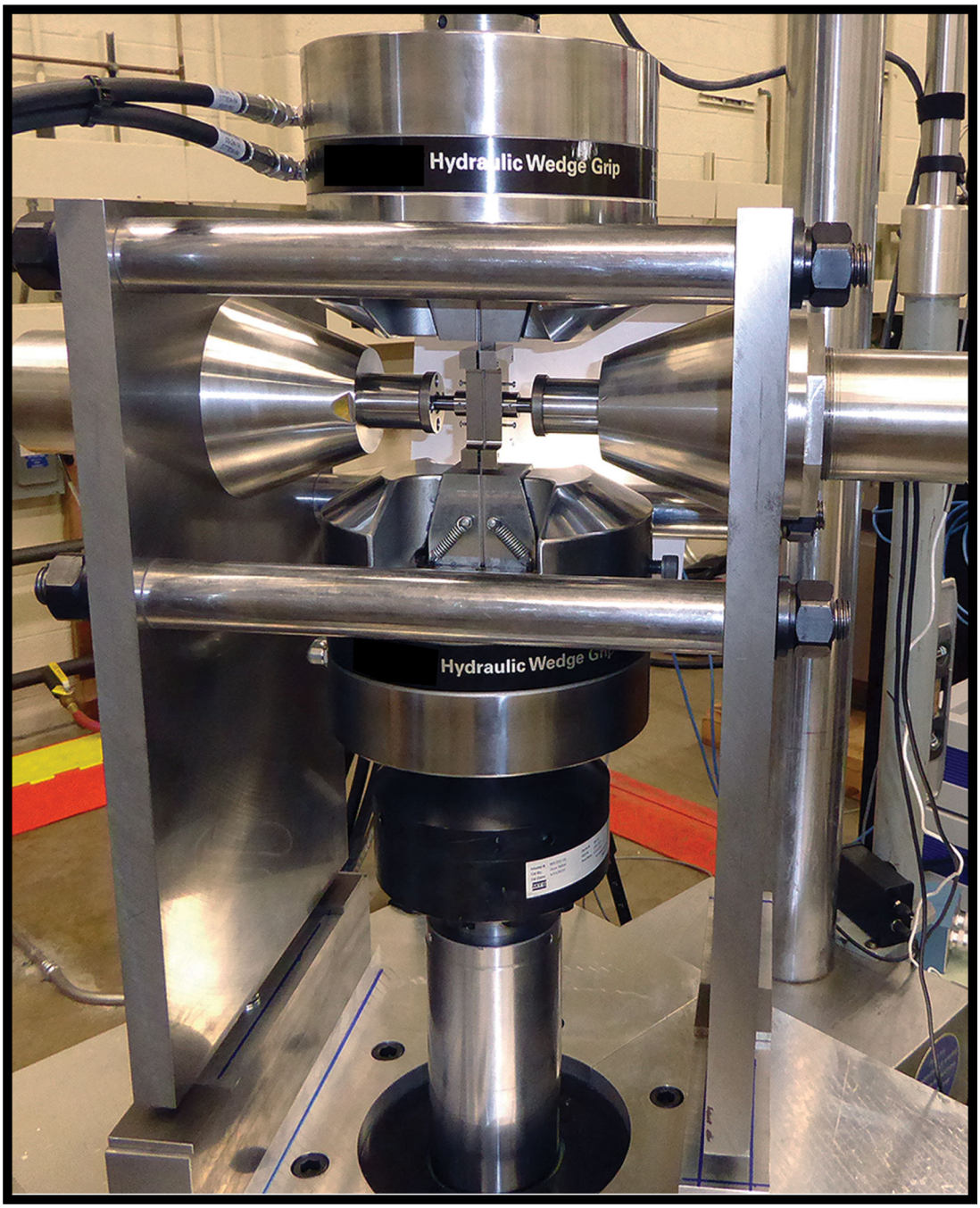


**Fig 2.**
The fully-assembled tension/compression test apparatus mounted in the servo-hydraulic load frame

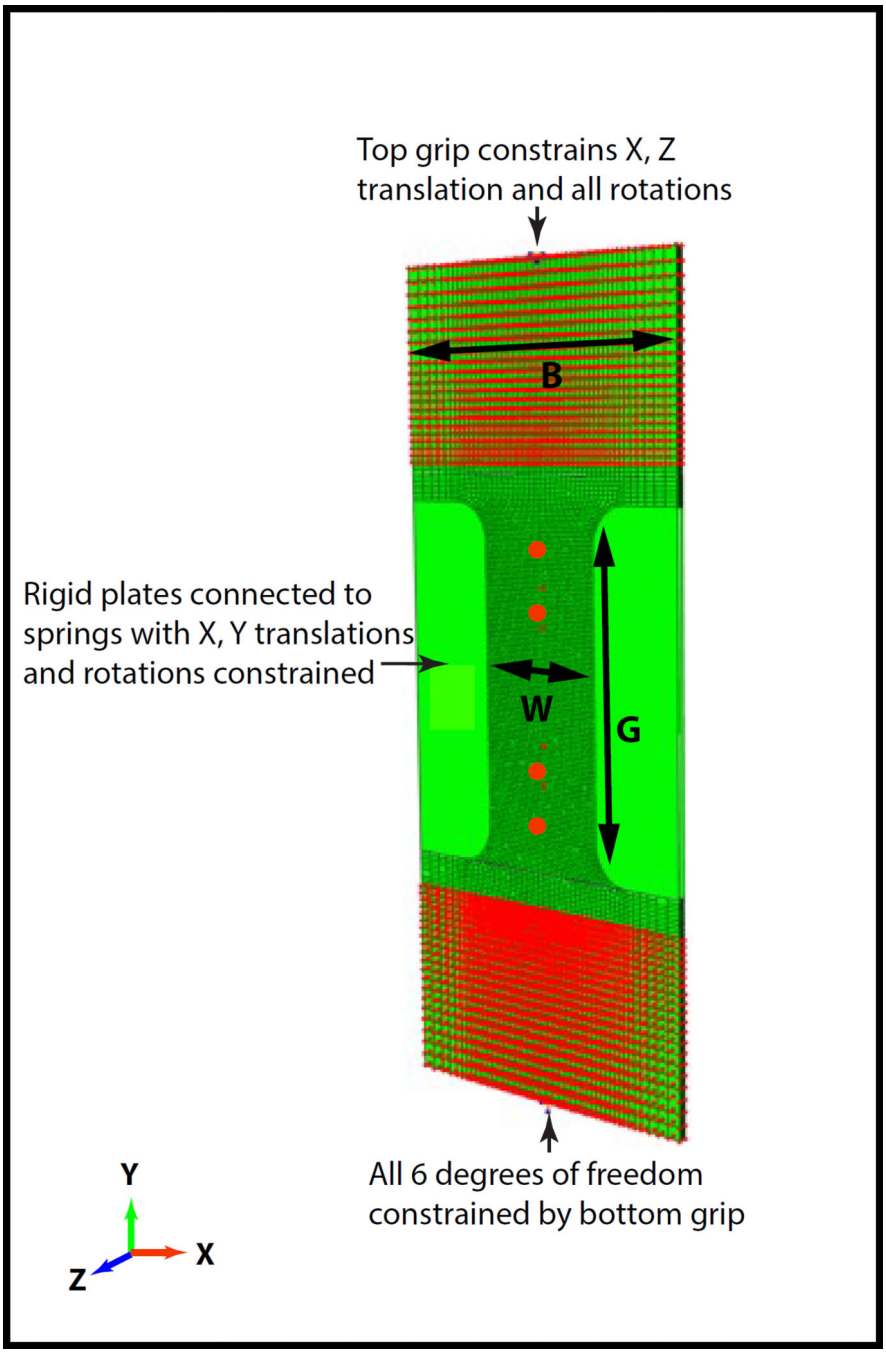


**Fig 3.**

The specimen geometry, mesh, and boundary conditions used for the FEA simulation of the behavior during fully-reversed loading. B is the tab width, W is the gauge width, and G is the gauge length

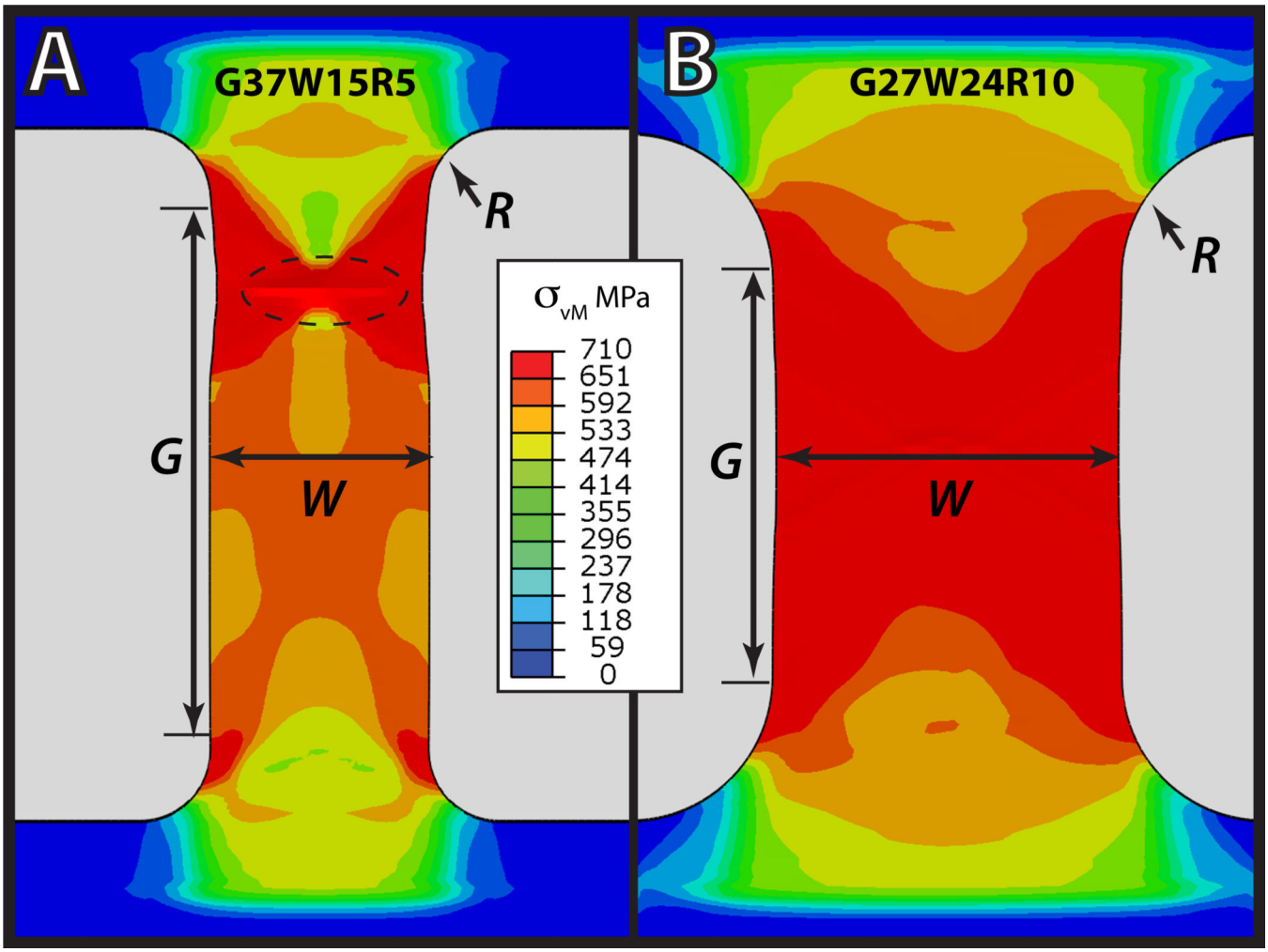


**Fig 4.**

The finite element-predicted performance for two different specimen geometries of DP600 over a ± 0.08-strain cycle (assuming isotropic hardening). G is the gauge length, W is the gauge width, and R is the radius. All dimensions are millimeters. The color bar is the von Mises stress in MPa

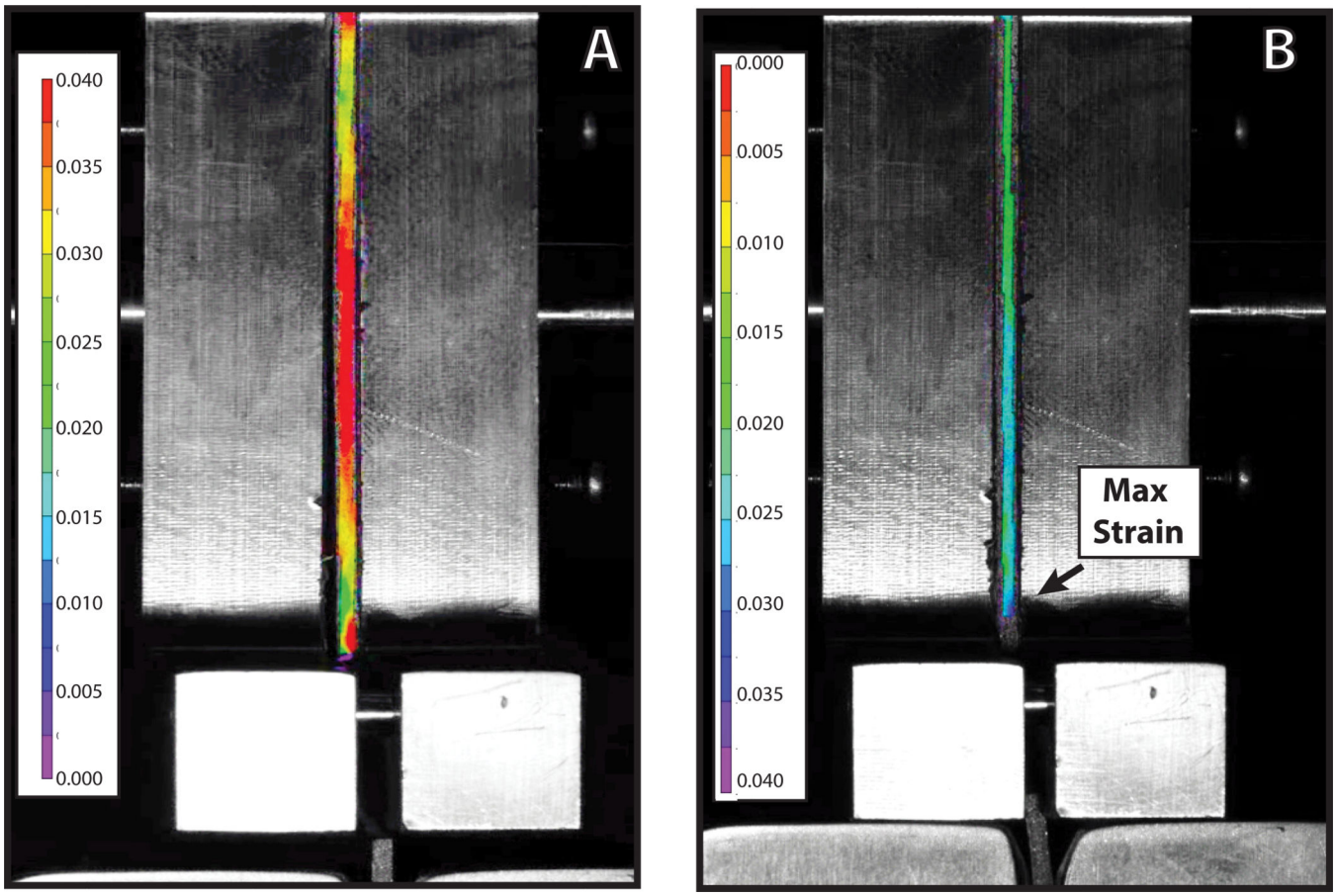


**Fig 5.**

Digital image correlation (DIC) data showing the Hencky strain distribution during the tension (Fig 5a) and compression (Fig 5b) segments of the fully-reversed 0.04 load cycle. The maximum tensile train was focused in the middle of the gauge section, but was more diffuse during compression. The maximum compression strain occurred closer to the actuator, which is seen at the bottom of the figure

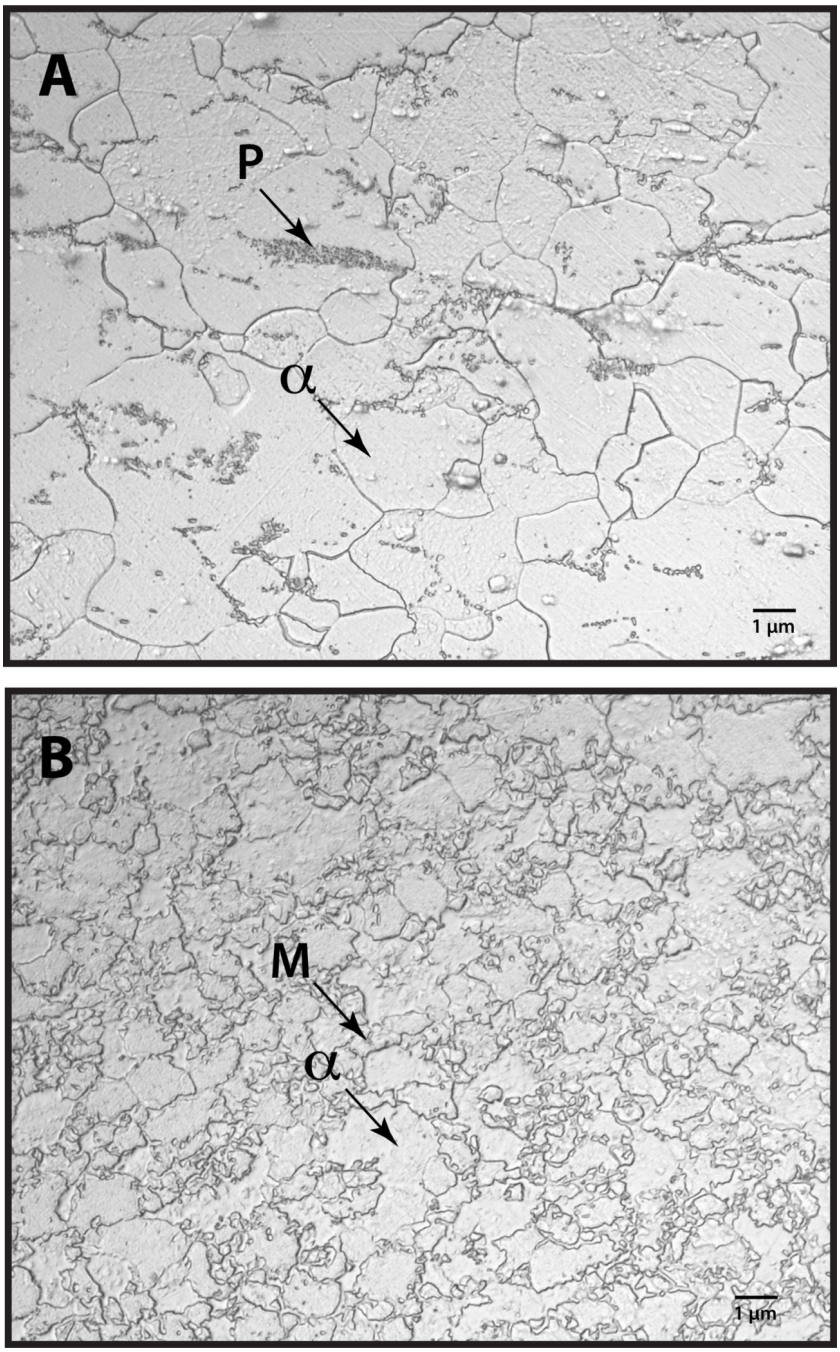


**Fig 6.**

Representative microstructures for the two steels. Fig 5a (AISI-1008) is a mixture of pearlite (P) and ferrite (α). Fig 5b (DP600) is a mixture of martensite (M) and ferrite (α). Both steels have similar carbon contents (≈ 0.85) (2% Nital etch)

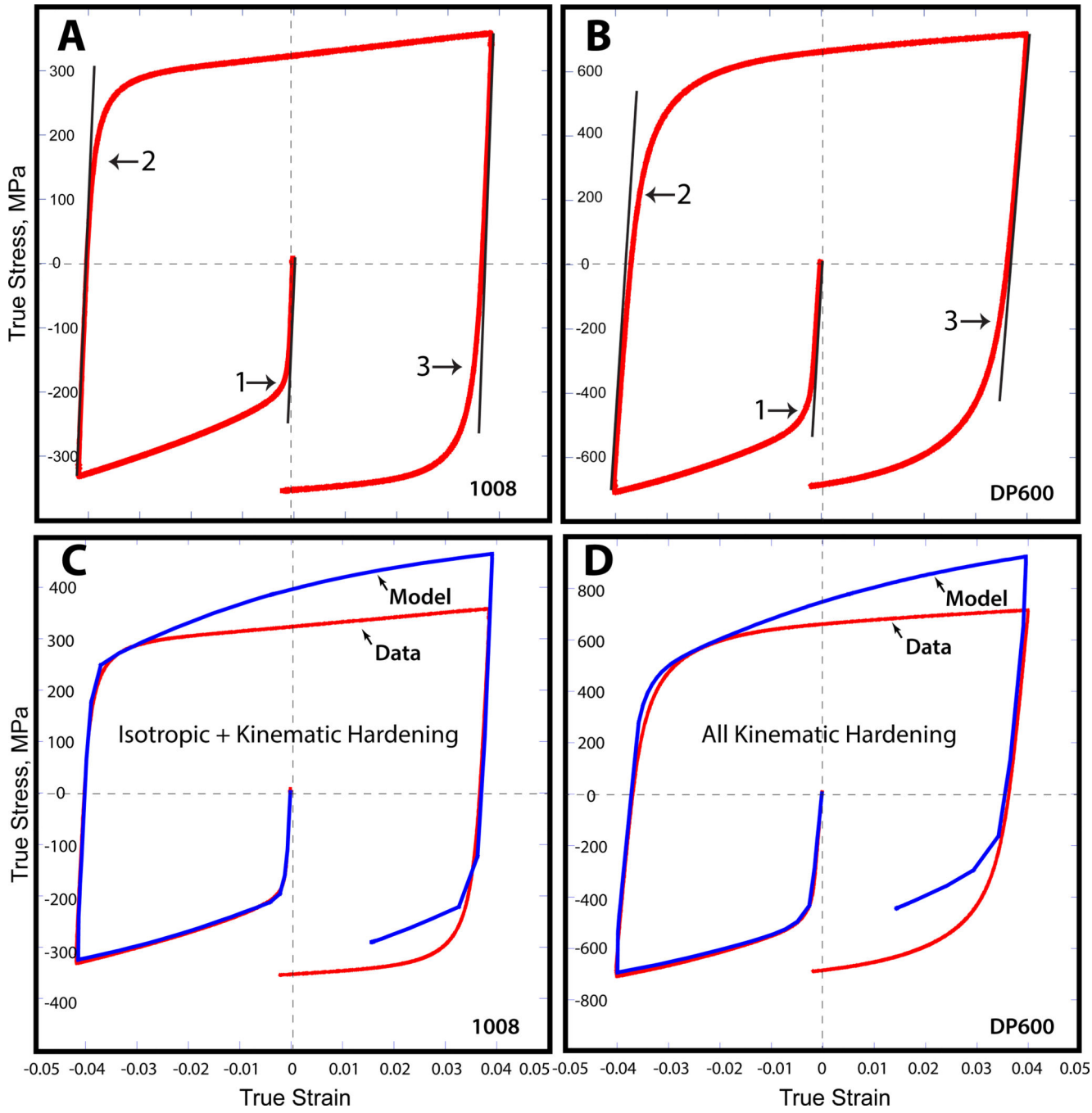


**Fig 7.**

The friction-corrected behavior of the two steels in ± 0.04 bidirectional loading. The AISI-1008 steel (Figs 7a and 7c) exhibits mixed isotropic/kinematic behavior over this strain cycle, whereas the DP600 (Figs 7b and 7d) exhibits primarily kinematic yield behavior. The 0.1 % offset yield points are shown in Fig 7a and 7b, and the simulation results using a nonlinear isotropic/kinematic hardening model are shown in Fig 7c and 7d

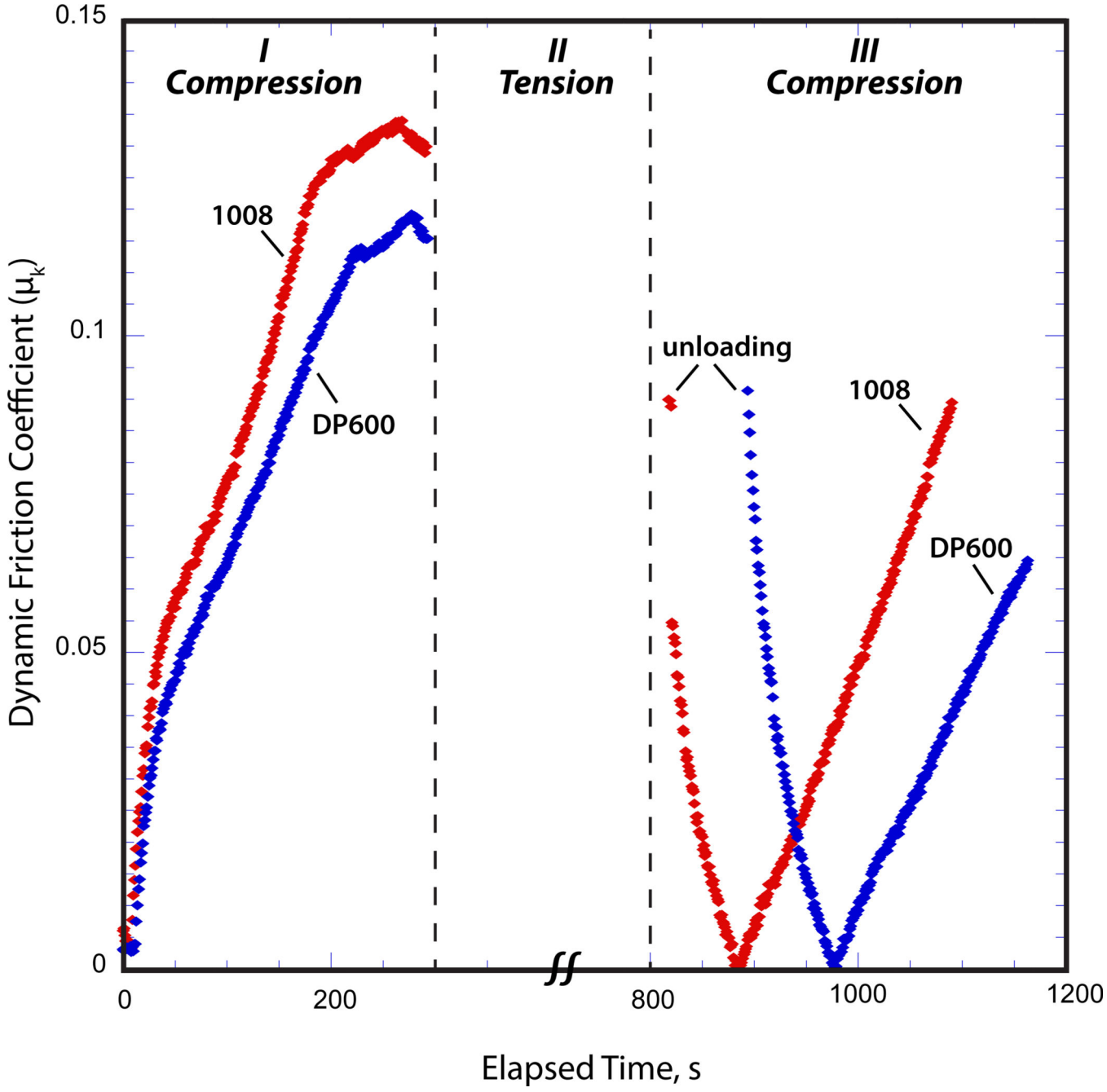


**Fig 8.**

The variation in the dynamic coefficient of friction for the two steels in bidirectional loading during the compression cycles when the anti-buckling guides were fully loaded. AISI-1008 steel exhibits an approximate maximum friction coefficient of 0.135, whereas the DP600 exhibits a maximum of 0.12 over the same ±0.04 strain range. Both maxima in $\mu_k$ occurred during the first compression segment (Region I).

**Table 1**

Yield Stress Behavior Using 0.1% Offset Criterion

| | AISI-1008 | DP600 |
|---|---|---|
| 1st Yield, MPa | −190 | −457 |
| 1st Maximum, MPa | −333 | −711 |
| 2nd Yield, MPa | +165 | +216 |
| 2nd Maximum, MPa | +357 | +713 |
| 3rd Yield, MPa | −175 | −182 |

(Measurement uncertainty ± 1 %)